

Densification of Titanium Diboride by Hot Isostatic Pressing and Production of Near-Net-Shape Components

J. Besson, F. Valin, P. Lointier, and M. Boncoeur

Hot isostatic pressing (HIP) was applied to the production of titanium diboride (TiB_2) parts. Cylinders were first produced to select the best starting powder (of two possible choices) and the processing conditions. Transverse strength, hardness, and toughness measurements were carried out on the densified products. Results were equivalent or better than data published in the literature, showing that HIP is an efficient method of processing ceramic powders. Constitutive equations representing the rheology of porous materials are presented and applied to the selected titanium diboride powder. Hot pressing and sinter forging tests were carried out to obtain the parameters of the constitutive equations. These equations were used in a finite-element program to simulate the forming of TiB_2 crucibles by HIP. These parts were actually processed using graphite or titanium inserts to produce a hollow, cylindrical part with a closed end. Observed and calculated final shapes were compared, showing good agreement. In addition, the finite-element program allowed the calculation of residual stresses after processing, of eventual remaining porosity. It then became possible to optimize processing routes, can, and insert geometries.

1. Introduction

IT is important for the optimization of processing of complex components by powder consolidation via hot isostatic pressing (HIP) or extrusion to be able to model the process using computer simulation techniques. This goal can be achieved by simultaneously developing constitutive equations describing the rheology of powder compacts and by using simulation tools such as finite-element method (FEM) programs. Hot isostatic pressing has potential for the fabrication of refractory ceramics, which are difficult to densify using more conventional processes such as sintering. In addition, lower temperatures can be used, thus allowing better control of the microstructure (fine grain size, for instance). Use of proper cans and inserts also allows the fabrication of complex geometries to near-net shape, which is especially interesting in the case of hard-to-machine materials.

In the present work, titanium diboride (TiB_2) powders were used to produce near-net-shape crucibles. The methodology is to:

- Produce fully dense bodies by HIP to demonstrate that this process produces materials of equal or better qualities than standard processes
- Study the rheological behavior of the ceramic powder and determine constitutive equations
- Use the constitutive model in a finite-element code to analyze density and stresses and forecast the final shape of the part
- Compare the calculation with actual data

J. Besson, Ecole Nationale Supérieure des Mines de Paris, Centre des Matériaux P.M. Fourt, Ecole des Mines de Paris, Evry Cedex, France; and **F. Valin**, **P. Lointier**, and **M. Boncoeur**, CEA/CEN Saclay, Yvette Cedex, France.

2. Rheology: Theory

Constitutive equations are presented below, which will be used to analyze the experimental data and to simulate forming processes such as HIP. At a macroscopic scale, the powder compact may be considered a continuous media with the relative density (ρ) as an internal variable. Several descriptions have been used to model the mechanical behavior of porous materials. Raj proposed to separate shear deformation and densification[1] and used this model in the case of alumina[2] and nickel aluminide powders.[3] When the creep law of the material is linear[4] (diffusion, viscous flow, etc.), it becomes possible to use the viscoelastic analogy; however, as noted by Bordia and Scherer,[5] this analogy cannot be easily used because physical moduli are not constant. Theoretical models have also been developed for linear viscoplastic materials,[6,7] for nonlinear viscous materials,[8] and for perfect plasticity.[9]

A more general, but phenomenological approach will be used in this study. It has been proposed and applied for the study of plastic and viscoplastic deformation of metal powders,[10-16] of ceramic powders,[17,18] and cold compaction of ceramic powders.[19] According to these studies, an effective stress (σ_{eff}) can be used, which accounts for the effect of porosity:

$$\sigma_{eff}^2 = 3c(\rho)J_2 + f(\rho)I_1^2 \qquad [1]$$

with

$$J_2 = \frac{1}{2}\tilde{s}:\tilde{s} \quad \tilde{s} = \tilde{\sigma} - \frac{1}{3}Tr(\tilde{\sigma})\tilde{1}$$

and

$$I_1 = Tr(\tilde{\sigma}) = \sigma_{11} + \sigma_{22} + \sigma_{33}$$

$\tilde{1}$: second-order unitary tensor

where c and f are decreasing functions of the relative density and represent the stress localization generated by the porosity; $\tilde{s}$ is the deviator of the stress tensor $\tilde{\sigma}$ and represents the shear applied to the material, and I_1 represents the pressure part of the stress tensor. Therefore, the effective stress can be separated into a shear part: $3cJ_2$ and a pressure part: fI_1^2. This allows for the modeling of both densification and shear deformation. The functions c and f must have the values $c = 1$ and $f = 0$ at full density ($\rho = 1$) so that the effective stress σ_{eff} is then equal to the Mises equivalent stress. It is also important to notice that the use of this kind of model implies that the basic mechanisms responsible for densification and creep (*i.e.*, shear deformation of the dense material) are the same; this hypothesis is, however, in agreement with microscopic densification models proposed in the literature.[20,21] To further develop the model, a normality rule between the viscoplastic strain rate tensor ($\dot{\tilde{\varepsilon}}_{vp}$) and the viscoplastic potential (Ω) is assumed. The strain rate tensor is then given by:*

$$\dot{\tilde{\varepsilon}}_{vp} = \frac{\partial \Omega}{\partial \tilde{\sigma}} = \frac{\partial \Omega}{\partial \sigma_{eff}} \frac{\partial \sigma_{eff}}{\partial \tilde{\sigma}} = \frac{1}{\sigma_{eff}} \frac{\partial \Omega}{\partial \sigma_{eff}} \left(\frac{3}{2} c\tilde{s} + fI_1 \tilde{1} \right) \quad [2]$$

An effective strain rate $\dot{\varepsilon}_{eff}$ can be defined, noting that the viscoplastic power (w) per unit volume is equal to:[3]

$$w = \tilde{\sigma} : \dot{\tilde{\varepsilon}}_{vp} = \rho \sigma_{eff} \dot{\varepsilon}_{eff} \quad [3]$$

According to Shima and Oyane,[13] w is not equal to $\sigma_{eff}\dot{\varepsilon}_{eff}$, because "a unit volume of a porous body with a relative density ρ consists of a matrix material of volume ρ." Using Eq 3, Eq 2 can be rewritten as (because $\dot{\varepsilon}_{eff} = (1/\rho)(\partial\Omega/\partial\sigma_{eff})$):

$$\dot{\tilde{\varepsilon}}_{vp} = \rho \frac{\dot{\varepsilon}_{eff}}{\sigma_{eff}} \left(\frac{3}{2} c\tilde{s} + fI_1 \tilde{1} \right) \quad [4]$$

* The notation $\dot{}$ denotes the time derivative: $\dot{x} = {}^{dx}/_{dt}$, where t represents the time.

σ_{eff} is given by Eq 1. Because it represents an effective stress acting in the dense matrix, $\dot{\varepsilon}_{eff}$ can be calculated using the creep law of the material: $\dot{\varepsilon}_{eff} = F(\sigma_{eff}, T)$, where T is temperature. It is interesting to note that this model is equivalent to the models proposed by Raj[1] and Scherer[6] when the material creeps linearly. When the material is nonlinear, there is an interaction between shear and pressure which implies that, for a given pressure, an additional shear stress enhances the densification.

Thermoelastic deformation is also taken into account. The total deformation rate is the sum of an irreversible part $\dot{\tilde{\varepsilon}}_{vp}$ (Eq 2) and of an elastic part $\dot{\tilde{\varepsilon}}_e$, which is given by (linear thermoelasticity):

$$\dot{\tilde{\varepsilon}}_e = \frac{1+\nu}{E} \dot{\tilde{\sigma}} - \frac{\nu}{E} Tr(\dot{\tilde{\sigma}}) \tilde{1} + \alpha \dot{T} \tilde{1} \quad [5]$$

where E is the Young's modulus, ν is the Poisson's ratio, α is the coefficient of thermal expansion, and T is temperature. Accounting for elastic deformations is necessary to calculate residual stresses after processing.

3. Experimental

3.1 *Powders*

Two powders (A and B) were chosen initially. The chemical analysis as stated by the supplier (Hermann C. Strack, Berlin) is given in Table 1. Grain size is 1.9 μm for powder A and 4.2 μm for powder B.

Table 1 Chemical Analysis of TiB_2 Powders

	Composition, wt%					
Powder	B	O	C	N	Fe	Ti
A	30.7	0.58	0.15	0.05	<0.15	bal
B	30.6	0.23	0.24	0.08	<0.10	bal

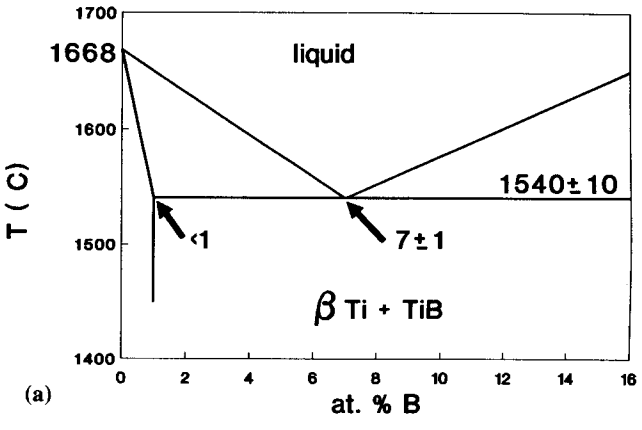

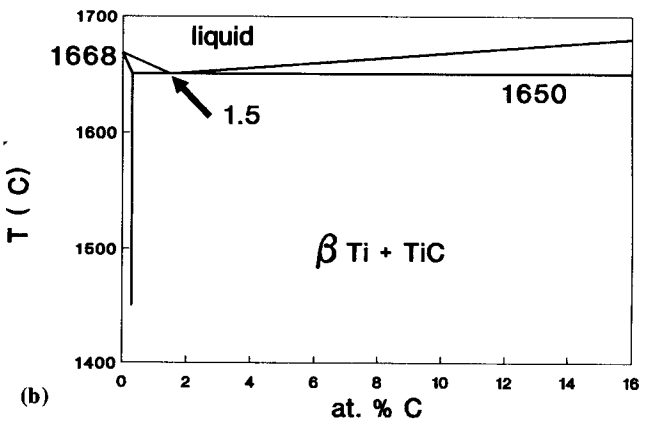

Fig. 1 Ti-B phase diagram (**a**). Ti-C phase diagram (**b**).[22]

3.2 *Encapsulation and HIP Densification*

Cylindrical containers made of pure titanium were used to densify the TiB_2 powders (thickness: 1 mm, diameter: 40 mm, height: 60 mm). A eutectic exists in the Ti-B phase diagram for an atomic concentration of B equal to 7%. The melting point is then 1540 °C (see Fig. 1a). It is therefore necessary to prevent a reaction between the canning material and the powder by using graphite foils and graphite spray as a chemical barrier. The Ti-C phase diagram is plotted in Fig. 1(b); it shows that the eutectic point is reached at 1650 °C. Hot isostatic pressing cycles were therefore performed at 1600 °C under a gas pressure (argon) of 200 MPa for 1 or 2 h (National Forge HIP 2000 apparatus). The heating rate was 20 °C/min. This rapid heating rate was chosen to quickly reduce the porosity so that full densification is achieved even if the container becomes leaky due to partial reaction with the TiB_2 powder.

Green preforms were produced either by cold isostatic pressing and subsequent machining, or by directly compacting the powder in the container. The initial green relative density was between 0.56 and 0.58. The container was outgassed at 600 °C (secondary vacuum), sealed under vacuum, welded, and HIPed. Final densities of both powders after HIP processing were measured using helium pycnometry. Under the previously mentioned conditions, relative densities above 99% were obtained.

Table 2 Young's Modulus of TiB_2 as a Function of Relative Density

Density, ρ	0.68	0.76	0.86	0.91	0.96	1.00
E, GPa	141	227	392	495	563	589

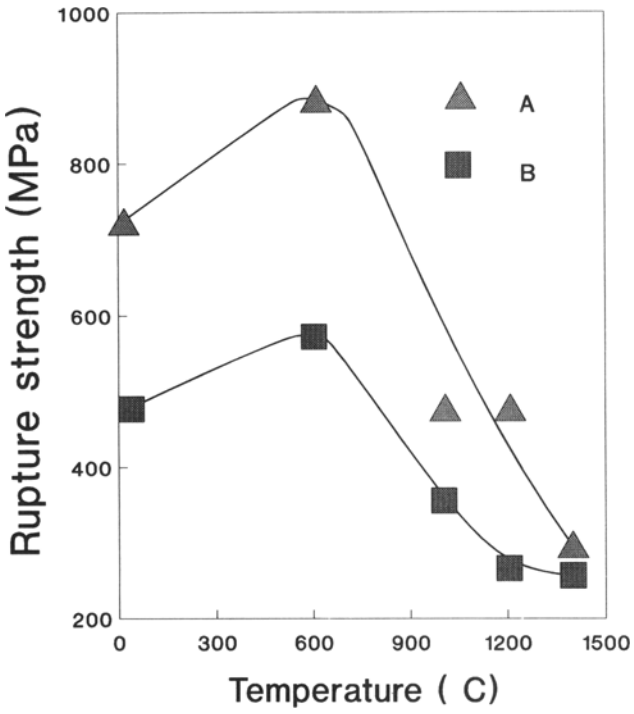

Fig. 2 Rupture strength of materials A and B as a function of temperature (three-point bending).

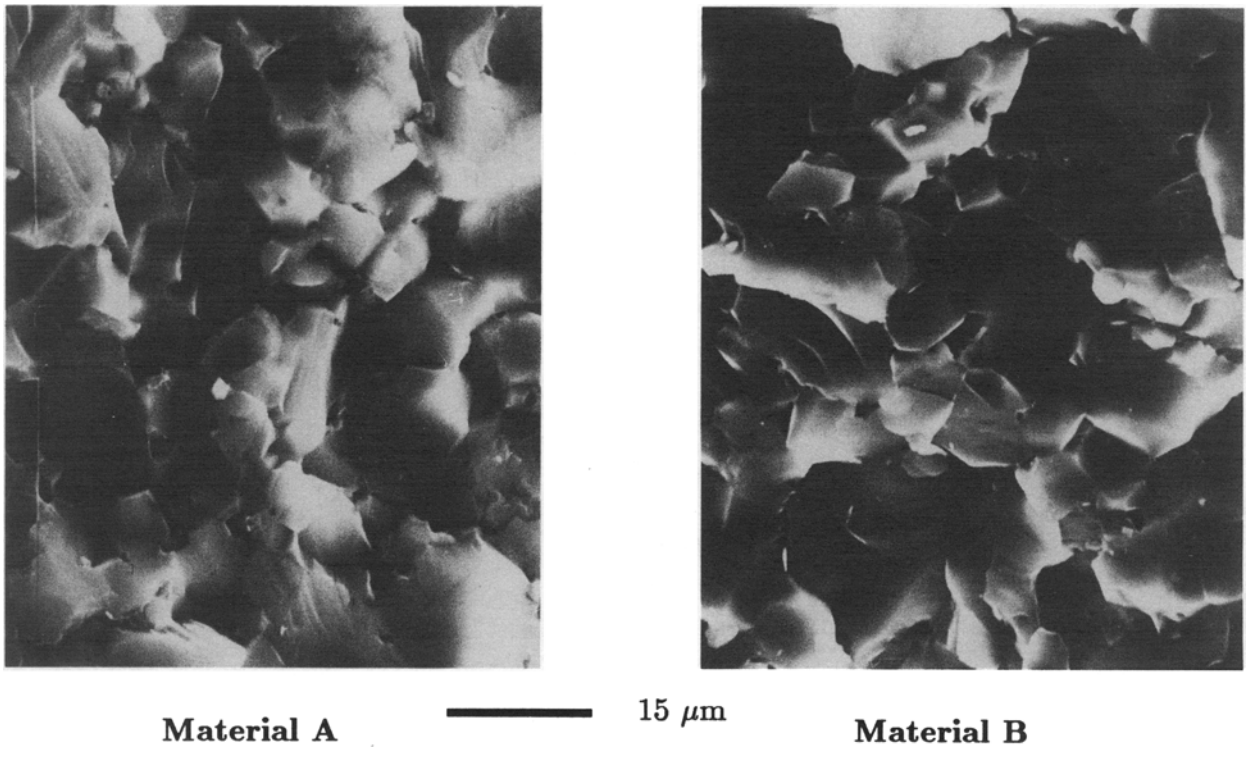

Fig. 3 Fractography of HIPed materials.

3.3 *Mechanical Characteristics of Densified Products*

3.3.1 *Elastic Properties*

Young's modulus and Poisson's ratio were measured at room temperature by a sonic-velocity method as a function of relative density. Results are shown in Table 2. Values obtained on the dense material were in good agreement with those published in the literature.[23-27] Poisson's ratio was constant; $\nu = 0.14$.

Table 3 Hardness and Toughness of Material A

Hardness (GPa) at 20 °C	$21 < H < 23$
K_{Ic} (MPa$\sqrt{m}$) at 25 °C	$4.9 < K_{Ic} < 5.2$
K_{Ic} (MPa$\sqrt{m}$) at 600 °C	$6.5 < K_{Ic} < 6.8$

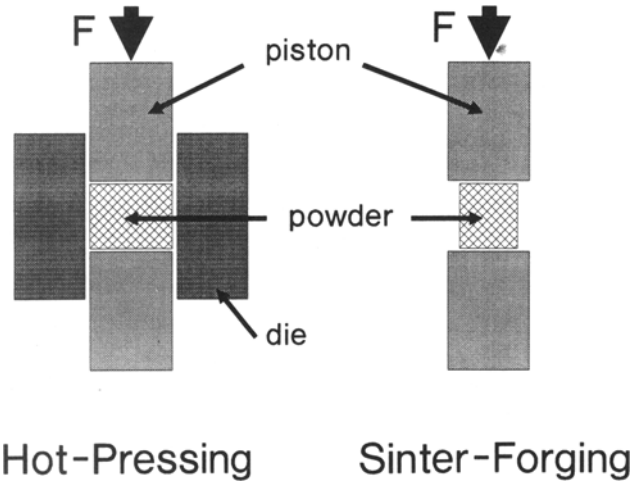

Fig. 4 Experimental setup of hot pressing and sinter forging operations.

3.3.2 *Fracture Strength*

Three-point bending tests were carried out in air for temperatures between 20 and 1400 °C using polished (7-μm) rectangular specimens of dimensions 20 by 4 by 2 mm. The fracture stress σ_f is related to the load (P) by:

$$\sigma_f = \frac{3}{2}\frac{PL}{be^2} \quad [6]$$

where L is the span (18 mm), b is the width, and e is the thickness of the sample. Results are summarized in Fig. 2 for both

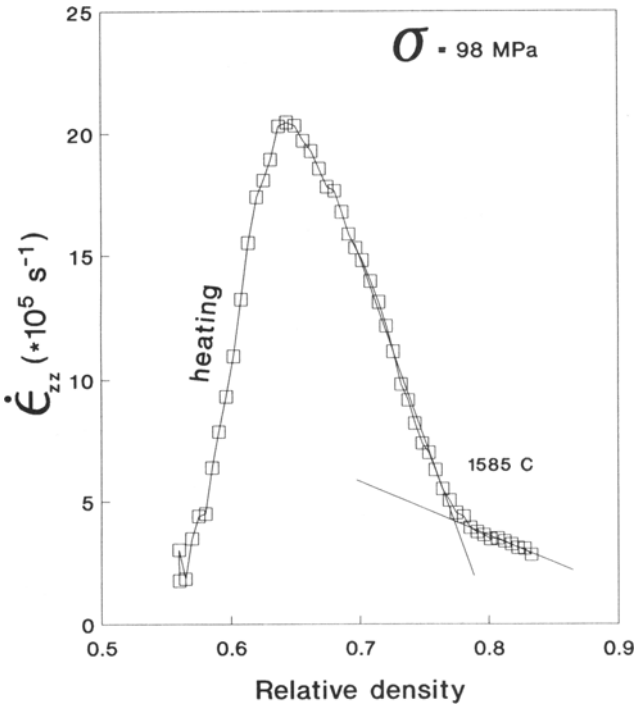

Fig. 5 Hot pressing test: deformation rate $\dot{\varepsilon}_{zz}$ versus relative density. The rapid decrease in the strain rate is due to the end of pore buckling ($\rho \cong 0.76$).

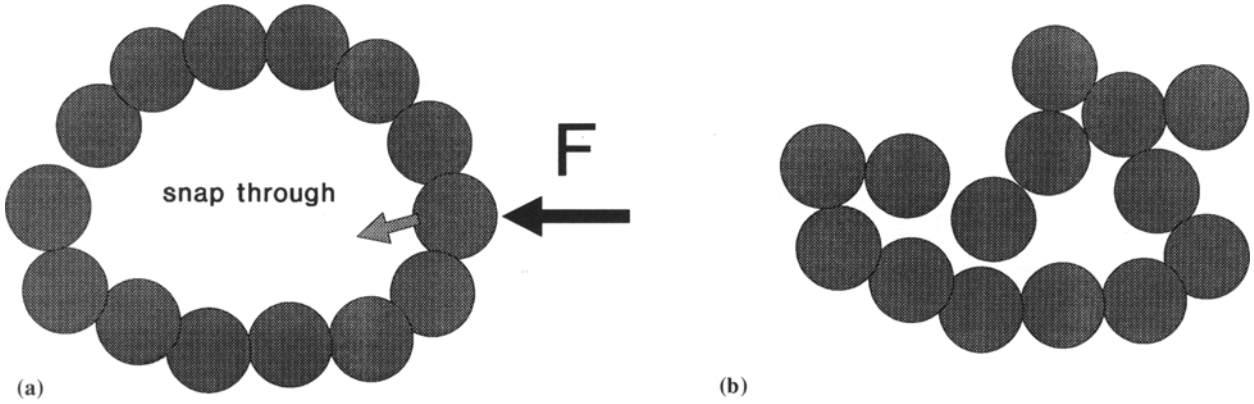

Fig. 6 Pore instability model.[32] **(a)** Initial configuration. **(b)** Particle snaps through and collapse ensues.

powders. For temperatures near 1400 °C, the specimens were oxidized rapidly. The apparent reinforcement at 600 °C can be explained by viscoplastic accommodation or microcracking near the crack tip.[28] This trend was in good agreement with results obtained by Baumgartner *et al.* on sintered TiB_2.[23] The fine grain size of powder A probably explains its superior resistance. Scanning electron microscope (SEM) examination of the fracture surfaces showed that rupture was mostly intergranular (Fig. 3). Note also that after HIP microstructure remained fine and isotropic.

3.3.3 *Hardness and Toughness*

Hardness was measured using the Vickers indentation technique on material A. Measurements were not possible on material B due to excessive chipping, which was probably related to the coarser grains of the material.[26] Precracked bars were then broken in three-point bending to estimate the fracture toughness (K_{Ic}) according to the procedure proposed by Chantikul *et al.*[29] K_{Ic} is given by:

$$K_{Ic} = 0.686\left(\frac{E}{H}\right)^{1/8}\left(\sigma_f P_i^{1/3}\right)^{3/4}$$

where H is the hardness, and P_i is the indentation load (4.2 kg); σ_f is given by Eq 6. Results are given in Table 3. The increase in K_{Ic} at 600 °C was in good agreement with the reinforcement observed at 600 °C in three-point bending. Experimental data on toughness of TiB_2 was in good agreement with the current experimental results.[26,27]

Because material A was stronger and tougher, the rheology of the powder and forming of parts was undertaken with powder A.

3.4 *Rheology: Experimental Procedure*

Hot pressing and sinter forging experiments (Fig. 4) were carried out in a vacuum furnace using graphite dies and pistons under constant load. Displacement of the pistons was measured by a linear variable differential transducer (LVDT). Temperature, load, and displacement were monitored continuously on a computer to analyze the data. The measured displacement was corrected for thermal expansion as well as for elastic deformation of the pistons. During hot pressing tests, the powder was directly cold pressed in the die before starting the experiment, and the load was maintained during heating. The die walls and the pistons were coated with graphite foils before each test to provide good lubrication. Samples, predensified by hot pressing at various relative densities, were used to carry out sinter forging tests. Radial displacement of the sample was not measured during sinter forging; it was assumed that the radial strain ε_{rr} was proportional to the axial strain ε_{zz}, so that:

$$\varepsilon_{rr} = \frac{\varepsilon_{rr}^t}{\varepsilon_{zz}^t}\varepsilon_{zz} \qquad [7]$$

where ε_{rr}^t and ε_{zz}^t are, respectively, the total radial and axial deformation measured after the experiment. ε_{rr} was used to calculate the stress σ in the powder during the test ($\sigma = \sigma_0 \exp(-2\varepsilon_{rr})$, where σ_0 is the initial applied stress), but it was not used to fit the constitutive equations. In some cases (high stress, low temperature), cracks and dedensification were observed during sinter forging. Because damage was not likely to occur during HIP, tests where damage was present were not considered when the parameters of the constitutive equations were determined. For stresses below 25 MPa and temperatures above 1600 °C, damage was not observed. In this case, the total axial strain varied between 5 and 20%, and barreling of the samples

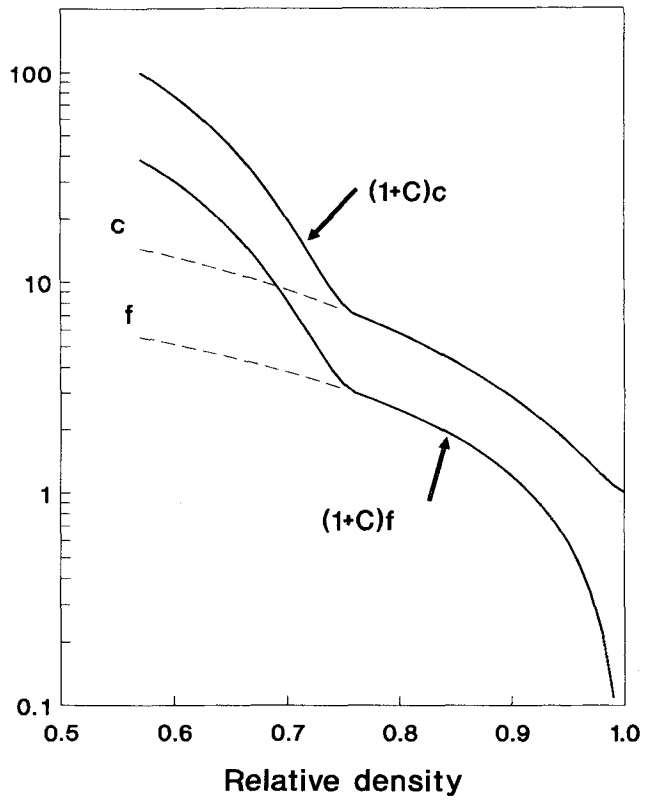

Fig. 7 Functions f, c, $(1 + C)f$ and $(1 + C)c$. For relative densities over 0.76 $C = 0$.

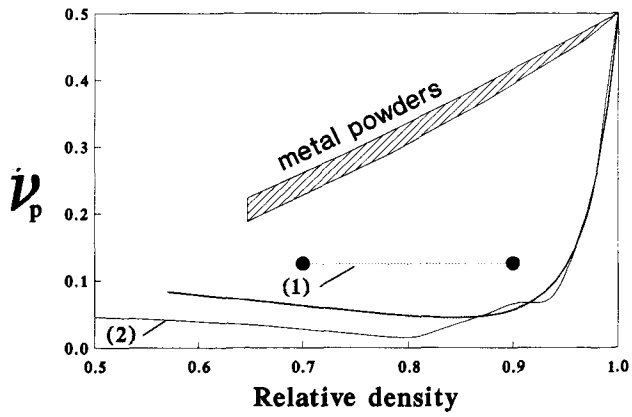

Fig. 8 Poisson's ratio of the TiB_2 powder (thick line) and comparison with experimental data for metals[11-15] and ceramics (1) (from Ref 2) and (2) (from Ref 18).

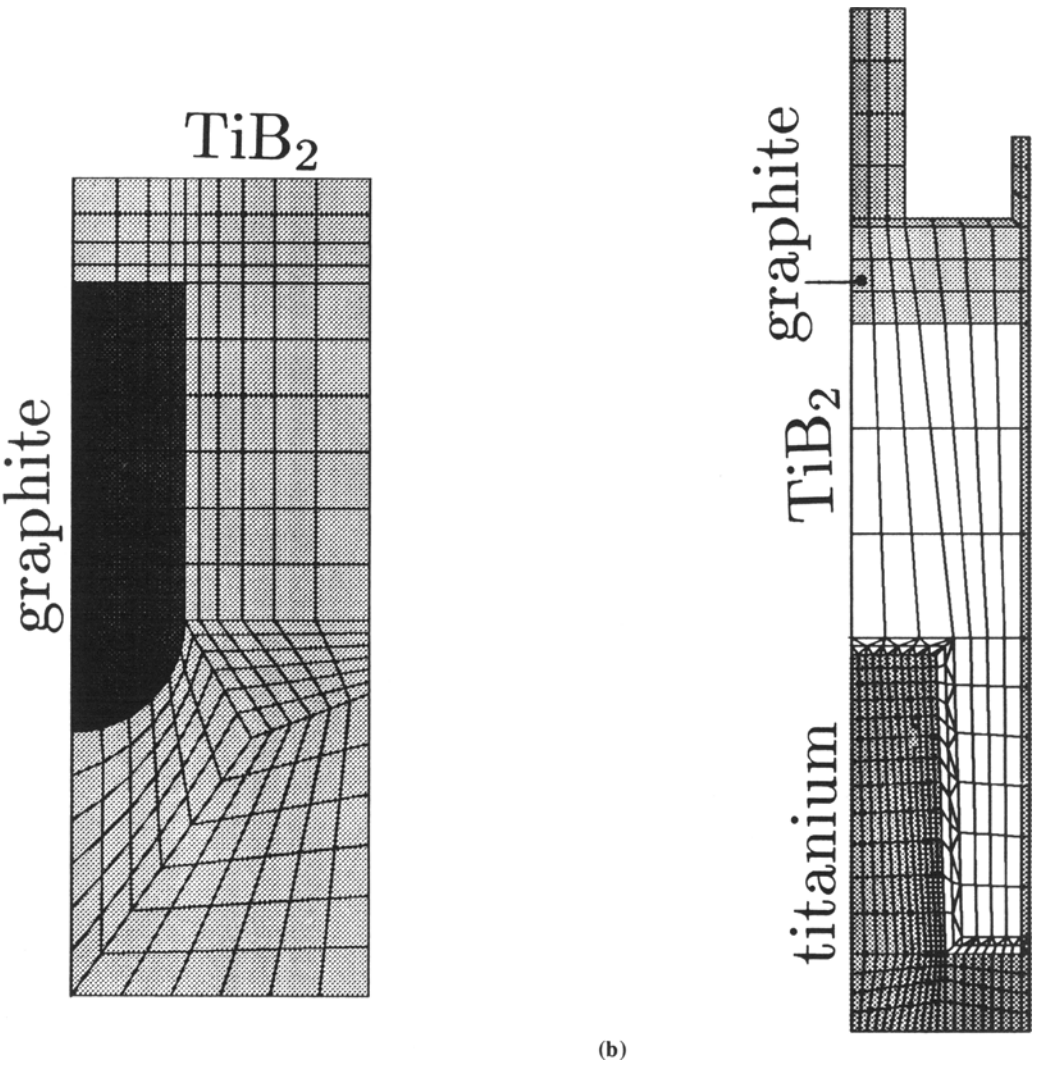

Fig. 9 Finite-element mesh used for the computations. (**a**) Graphite core method (232 elements, 749 nodes). (**b**) Titanium core method (411 elements, 1260 nodes).

was negligible. This was mainly due to the fact that the radial expansion of the sample was very limited. In all cases, the load was maintained during heating (heating rate 20 °C/min). This testing schedule was chosen to test the material in conditions as close to those encountered during HIP processing (see above).

Adjustment of the parameters of the constitutive equations was performed using an automatic curve-fitting program that minimizes the total difference Δ between the theoretical and experimental axial deformation rates during hot pressing and sinter forging.

$$\Delta = \sum_{\text{experimental data}} (\dot{\varepsilon}_{zz}^{\text{theoretical}} - \dot{\varepsilon}_{zz}^{\text{experimental}})^2 \quad [8]$$

Using the previously described model, the deformation rates are given by:

$$\begin{cases} \dot{\varepsilon}_{zz} = \rho\Gamma \dfrac{9fc}{c+4f}\sigma_{zz} \text{ hot pressing} \\ \dot{\varepsilon}_{zz} = \rho\Gamma(c+f)\,\sigma_{zz} \text{ sinter forging} \\ \text{with } \Gamma = \dot{\varepsilon}_{\text{eff}}/\sigma_{\text{eff}} \end{cases} \quad [9]$$

4. Rheology: Experimental Results

Experimental data were analyzed using Eq 9 and the automatic adjustment program based on Eq 8. Therefore, the stress localization functions c and f were fitted together with the parameters of the creep law. Both hot pressing and sinter forging tests must be used to determine those two functions. Curve-fitting appears to be necessary to closely represent the experiments and to simulate the HIP process.

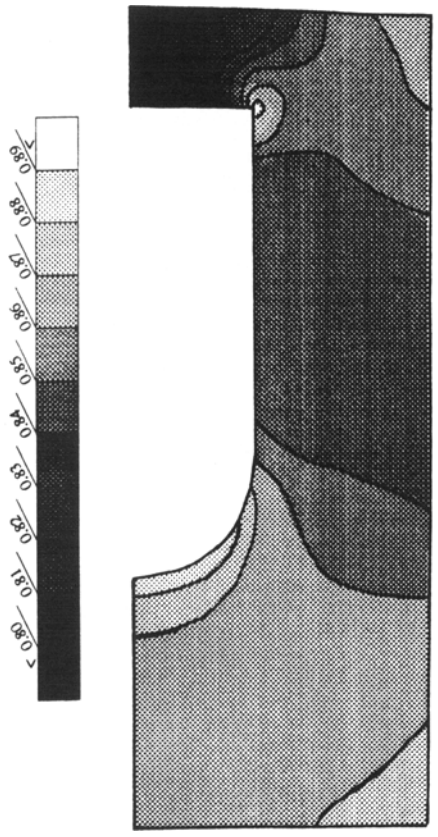

Fig. 10 Density map (%) at the beginning of the HIP dwell (graphite core).

4.1 *Stress Localization Functions f and c*

It was experimentally observed that densification during hot pressing (σ = 50 to 100 MPa) begins at relatively low temperatures (1200 to 1300 °C). In addition, densification behavior drastically changes for relative densities over 0.76. An example is given in Fig. 5. The same trends have been observed on an alumina powder tested under the same conditions.[18] This phenomenon can be interpreted as follows. At low density, large voids exist in porous ceramic preforms.[30,31] Due to local high forces between touching particles, these voids can collapse.[32] This results in very high densification rates. The buckling/rearrangement mechanism is shown in Fig. 6. To account for buckling and rearrangement, Eq 2 was modified as follows:

$$\dot{\tilde{\varepsilon}}_{vp} = \frac{1}{\sigma_{eff}} \frac{\partial \Omega}{\partial \sigma_{eff}} (1 + C) \left(\frac{3}{2} c \tilde{s} + f I_1 \tilde{1} \right) \qquad [10]$$

where C is a coefficient depending on the relative density, which accounts for low density buckling. The physical phenomenon responsible for deformation while the pores are buckling is supposed to be the same as the mechanism responsible for final densification (high density). This mechanism is likely to be diffusional creep. The porous structure creeps so that particles move until the pore becomes unstable and collapses. Local stresses acting between particles are responsible for both movements generating interpenetration of particles (stage I of densification[21]) and shrinkage of voids (stage II) and movements resulting in void collapse. Therefore, it is consistent to use σ_{eff} (which accounts for local stresses) to describe densification by pore buckling as well as stage I and II densification. C accounts for the accelerated macroscopic deformation due to buckling. The curve-fitting program gives the following expressions for f, c, and C:

$$f = [11.9(1 - \rho)]^{1.04}$$
$$c = 1 + [15.9(1 - \rho)]^{1.35}$$
$$C = 10.85 \langle 0.76 - \rho \rangle^2 \exp(4.72\rho) \qquad [11]$$

where $\langle x \rangle$ is equal to 0 $x < 0$ and to x if $x > 0$. Therefore, for densities above 0.76, rearrangement does not occur. f and c as well as $(1 + C)f$ and $(1 + C)c$ are plotted in Fig. 7.

An insightful parameter is the plastic Poisson's ratio ν_p defined as the ratio of the radial deformation rate to the axial deformation rate during sinter forging:

$$\nu_p = \frac{1}{2} \frac{c - 2f}{c + f} \qquad [12]$$

For $\rho = 1$, the material is incompressible so that $\nu_p = \frac{1}{2}$; ν_p is also usually considered to be greater than 0 because it is unlikely to observe a radial shrinkage during forging.[4] The Poisson's ratio is shown in Fig. 8. The Poisson's ratio of the TiB_2 powder is systematically smaller than the values reported on metal powders in the literature. On the other hand, these results are close to what was observed on alumina.[2,18] (See Ref 18 for the calculation of ν_p for data given in Ref 2.) These data show that ν_p is very close to 0 for relative densities between 0.5 and 0.9. Therefore, the radial expansion during sinter forging will be very limited, as has been observed.

4.2 *Creep Law*

The creep law of the material is supposed to be given by:

$$\dot{\varepsilon}_{eff} = A \exp(-Q/RT) \sigma_{eff}^n \qquad [13]$$

where Q is the activation energy, and n is the stress exponent. A, Q, and n are used as fitting parameters. The least-square adjustment procedure gives the following results:

$$\begin{cases} A = 875{,}000 \ s^{-1} \ \text{MPa}^{-n} \\ Q = 480 \ \text{kJ} \cdot \text{mol}^{-1} \\ n = 1.35 \end{cases}$$

Experimental data on creep and densification of TiB_2 is very limited. Koval'chenko[33] reported an activation energy of 610 kJ · mol^{-1} for a powder of commercial purity and of 480 kJ · mol^{-1} for a powder containing 0.1 wt% Fe; the stress exponent is equal to 2. The test temperature was between 2100 and 2400 °C and stresses between 5 and 15 MPa. The same stress exponent was reported for a $(Ti,Cr)B_2$-base alloy processed at lower temperatures.[34] Results obtained by Finch *et al.*[25] show that densification near full density can be obtained at 1600 °C using a pressure of 35 MPa and a holding time of 2 hr on a powder having a 2- to 10-μm grain size. Clougherty *et al.*[35] obtained

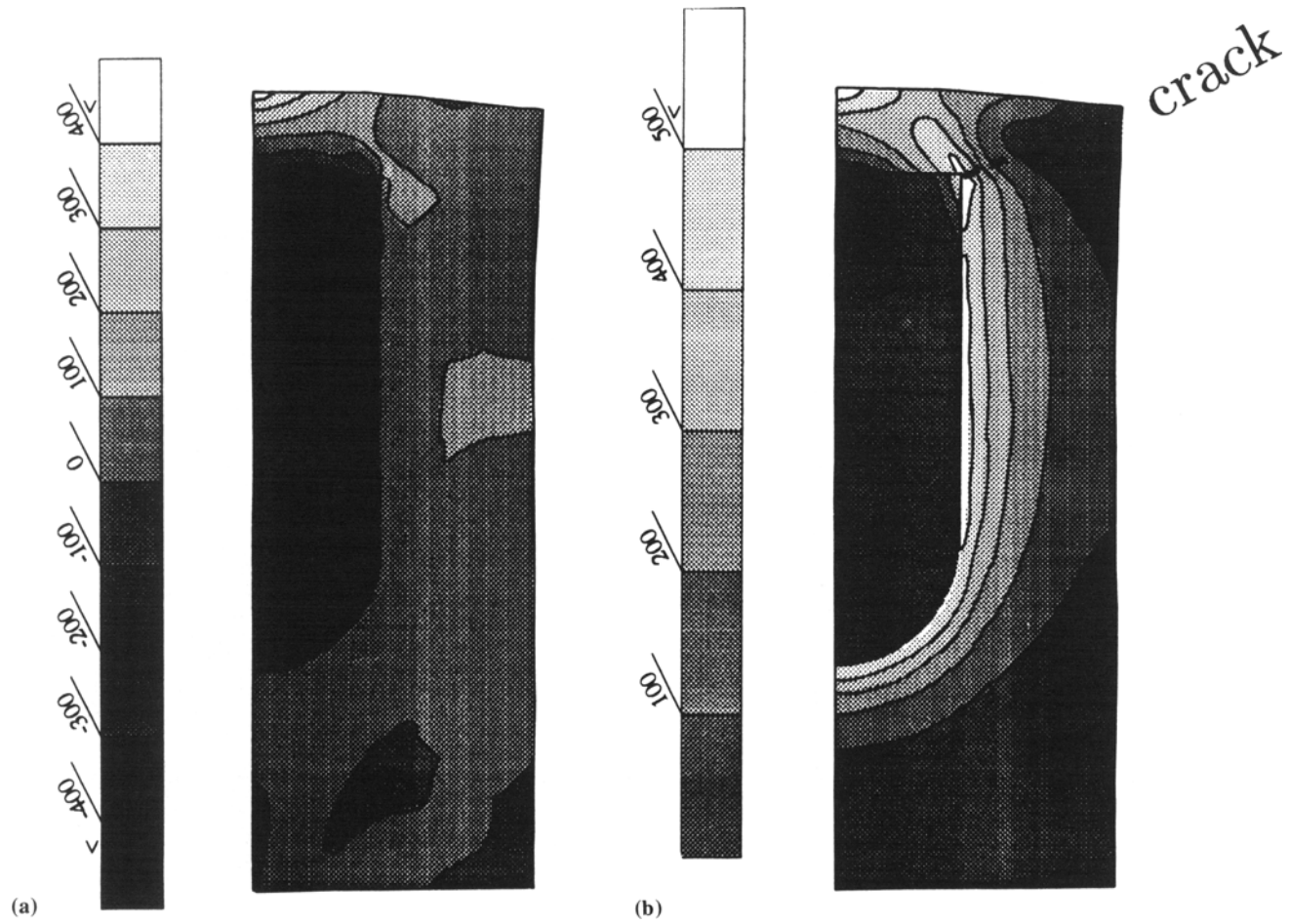

Fig. 11 Stress maps (MPa) at the beginning of the HIP dwell (graphite core). (**a**) Pressure ($I_1/3$). (**b**) Shear ($\sqrt{3J_2}$) (graphite core).

similar results at 1600 °C with higher pressures (1500 to 2000 MPa), but shorter holding times (6 to 18 min). The current experimental results are in relatively good agreement with the findings of Koval'chenko *et al.*[33,34] and the densification kinetics observed by Finch *et al.*[25] Low stress exponents are usually found in ceramic because diffusional creep, rather than dislocation creep, controls the deformation mechanisms.[36]

5. Simulation of HIP/Near-Net-Shape Forming

TiB_2 crucibles were made with powder A. They consisted of a cylinder with an internal hole with a closed end. To avoid machining (especially drilling of the central hole), HIP was used to produce the crucibles to near-net shape. The central hole was produced using an insert; two methods were considered: a graphite core and a titanium core.[37] Both techniques were analyzed by simulating the forming process using the finite element method (FEM). The main problems encountered during processing were: (1) poorly controlled deformation of the powder due to stiffening effects of the can and of the insert,[38-40] and (2) residual stresses after cooling due to thermal expansion mismatch between the canning material, the powder, and the insert. TiB_2 has a thermal expansion coefficient of $8.3\ 10^{-6}\ K^{-1}$.[27]

5.1 *Finite-Element Computation*

The constitutive equations were used in a FEM simulation program to model the deformation of cans filled with powder during HIP. The program used Zébulon software developed by the Centre des Matériaux de l'Ecole des Mines de Paris. Algorithms used in the program were presented elsewhere.[11] Elements used for the calculations were isoparametric triangles (six nodes, six Gauss points) or rectangles (eight nodes, nine Gauss points). The computing strategy was based on an implicit scheme.[11] Incremental strains and displacements remained small, and the geometry was updated after each time increment. Due to the small size of the samples, the temperature was supposed to be uniform in the container and equal to the gas temperature. The HIP pressure was imposed on the free surfaces.

5.2 *Graphite Core Method*

A graphite insert was introduced in the powder compact to obtain the hollow cylinder. The bottom of the insert was ma-

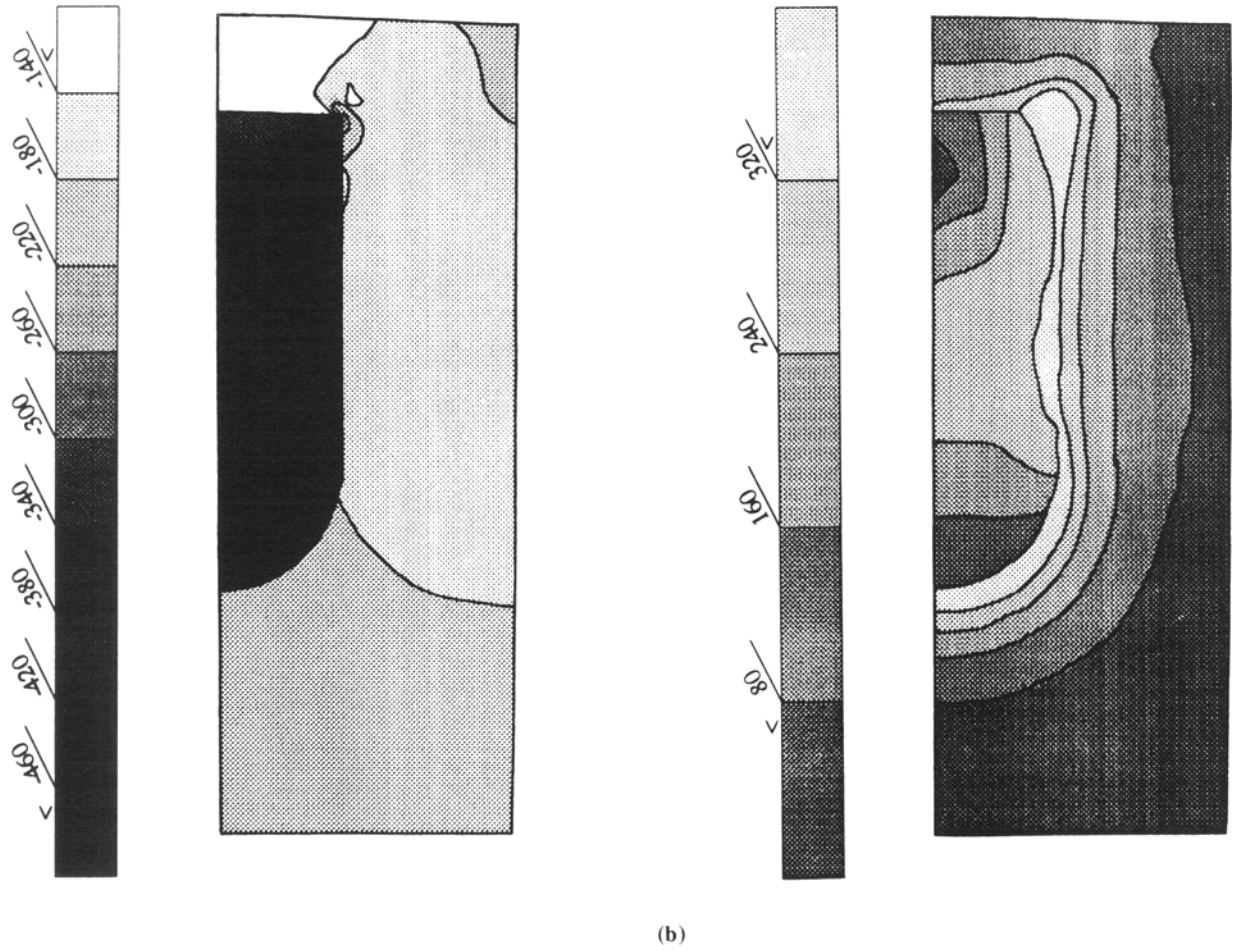

Fig. 12 Stress maps (MPa) after cooling (graphite core). **(a)** Pressure ($I_1/3$). **(b)** Shear ($\sqrt{3J_2}$) (graphite core).

chined to a half sphere to avoid cracking after cooling. The top of the insert had sharp edges and cracks propagated. The titanium can was neglected and the graphite insert was modeled as a pure thermoelastic body (Young's modulus, 9800 MPa; Poisson's ratio, 0.07; thermal expansion coefficient, $3.10^{-6}\,K^{-1}$).

The FEM mesh used for the computation is shown in Fig. 9(a). Figure 10 represents the map of densities at the beginning of the pressure and temperature dwell (200 MPa, 1600 °C). A gradient of densities existed ($0.80 < \rho < 0.90$). Figure 11 represents the map of pressure ($I_1/3$) and shear ($\sqrt{3J_2}$) at the same time. The pressure in the powder was lower than the external applied pressure, but it was much higher in the insert (≅500 MPa) so that the global mechanical equilibrium was maintained. Shear reached a maximum at the interface between the graphite core and the powder. Pressure and shear gradients generated by the insert accounted for the density gradient. At the end of the HIP dwell, full densification was achieved in the entire sample; pressure was uniform and shear was close to zero.

Both constituents (graphite and TiB_2) were subjected to residual stresses after cooling. Figure 12 represents the stress maps after cooling. Neither the graphite core nor the ceramic accommodated the thermal mismatch by plastic flow to reduce residual stresses. On the other hand, the low Young's modulus of graphite allowed the core to deform easily so that tension stresses in the ceramic remained less than the experimental fracture stress thus allowing safe crucibles to be produced. Near the sharp edge of the core, stresses were very high so that a "cup/cone"-like fracture occurred.

5.3 *Titanium Core Method*

Creep, plasticity, and thermoelastic (Young's modulus, Poisson's ratio, thermal expansion coefficient, thermal conductivity, and specific heat) data for the canning material were taken from the literature.[36,41] A graphite insert was also introduced at the top of the container. The FEM mesh is shown in Fig. 9(b). The actual final container is shown in Fig. 14. The density map at the beginning of the dwell is represented in Fig. 13, showing a large density gradient that is related to the pressure gradient (Fig. 15). The shear stress was large close to the noncreeping graphite insert, but very low in the titanium, which flows easily (Fig. 15). During cooling, the outer thin titanium shell yielded easily. The inner core had a larger coefficient of thermal expansion than the surrounding TiB_2 ceramic so that

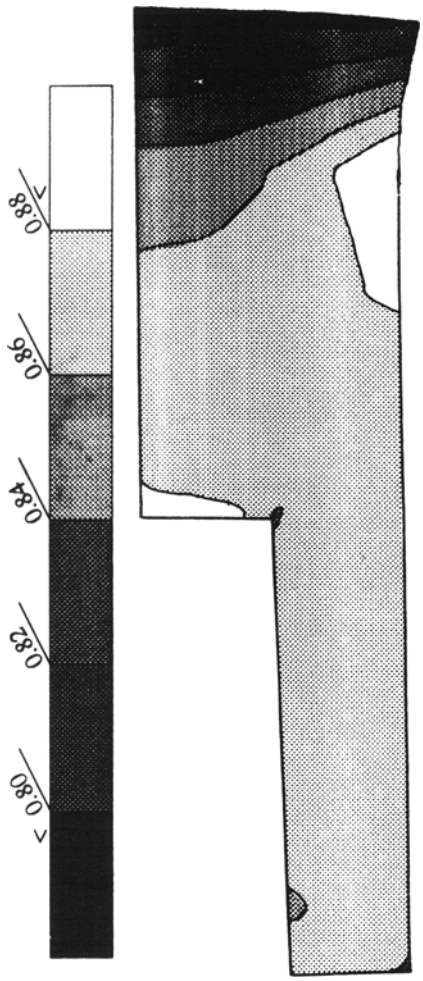

Fig. 13 Density map (%) at the beginning of the HIP dwell (titanium core).

debonding occurred. The graphite foil facilitated debonding. Modeling of debonding was not carried out. An estimation of the stresses can be calculated considering a hollow elastic body surrounded by a perfectly plastic shell (see Ref 42).

Experimental and calculated final shapes are shown in Fig. 16. Good or excellent agreement was found, particularly considering the shape of the TiB_2 crucible. Observed differences can be accounted for by the presence of the protective graphite foil or by slightly inaccurate machining of the green bodies. The final shape was also compared to the shape forecasted by simply assuming that the densification is isotropic (Fig. 16b). Differences are larger, but still remain small compared to the size of the ceramic part. This shows that the influence of the titanium core on the densification of the crucible was very limited; titanium roughly behaved like an incompressible fluid between 1500 and 1600 °C. During densification, the titanium core is extruded out of the ceramic and produces a bulge (Fig. 16c). The calculation overestimates the bulging effect. Several hypotheses could, however, account for the rounding of the bulge during holding at 1600 °C: (1) weight of the structure, (2) surface diffusion, or (3) partial melting.

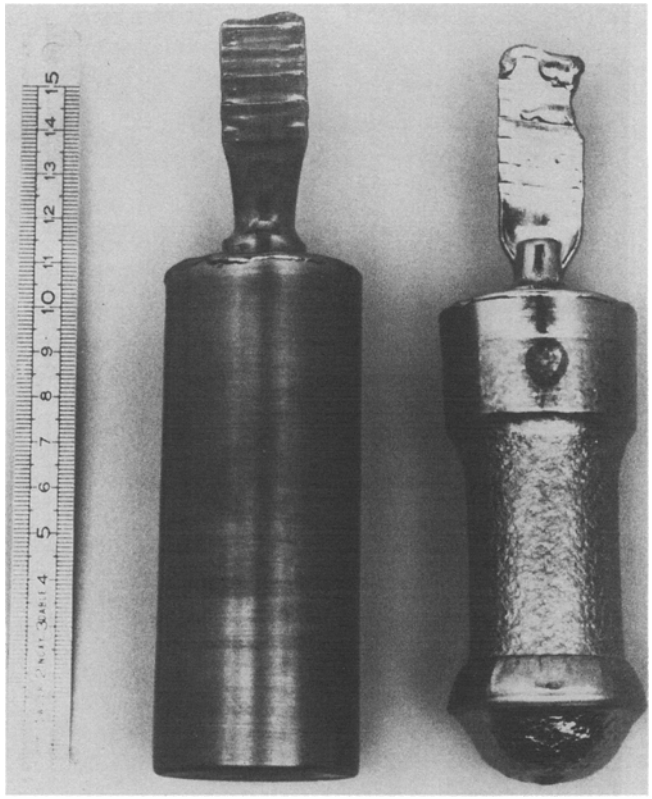

Fig. 14 Final container (titanium core).

6. Concluding Remarks

Powder compacts and crucibles of pure TiB_2 were HIPed at 1600 °C under 200 MPa to full density. The rheology of the powder was investigated, and the mechanical properties of the dense product were measured. The following results were obtained.

The dense materials have mechanical properties (toughness, hardness, and rupture strength) that are equal to or better than the properties published in the literature obtained on similar materials processed by sintering or hot pressing at higher temperatures, lower pressure, with or without sintering additives.[23-27] Hot isostatic pressing appears to be an efficient way to produce high-quality ceramic.

The rheological behavior of the TiB_2 powder was comparable to what has been previously observed on alumina.[2,17,18] This behavior drastically differs from what has been measured on metallic powders.[10-14,21]

Crucibles (cylinder with an internal hole) were produced using two different techniques. A graphite insert was used to produce the central hole. In spite of the large thermal expansion mismatch between the graphite and TiB_2, a sound part can be produced due to the low Young's modulus of the graphite. A titanium insert was also used to produce the central hole. Residual stresses after processing were very limited due to both debonding between the titanium core and the ceramic and plastic yielding of the outer thin titanium shell.

The FEM calculation was used to simulate the densification process; estimations of density gradients during processing and

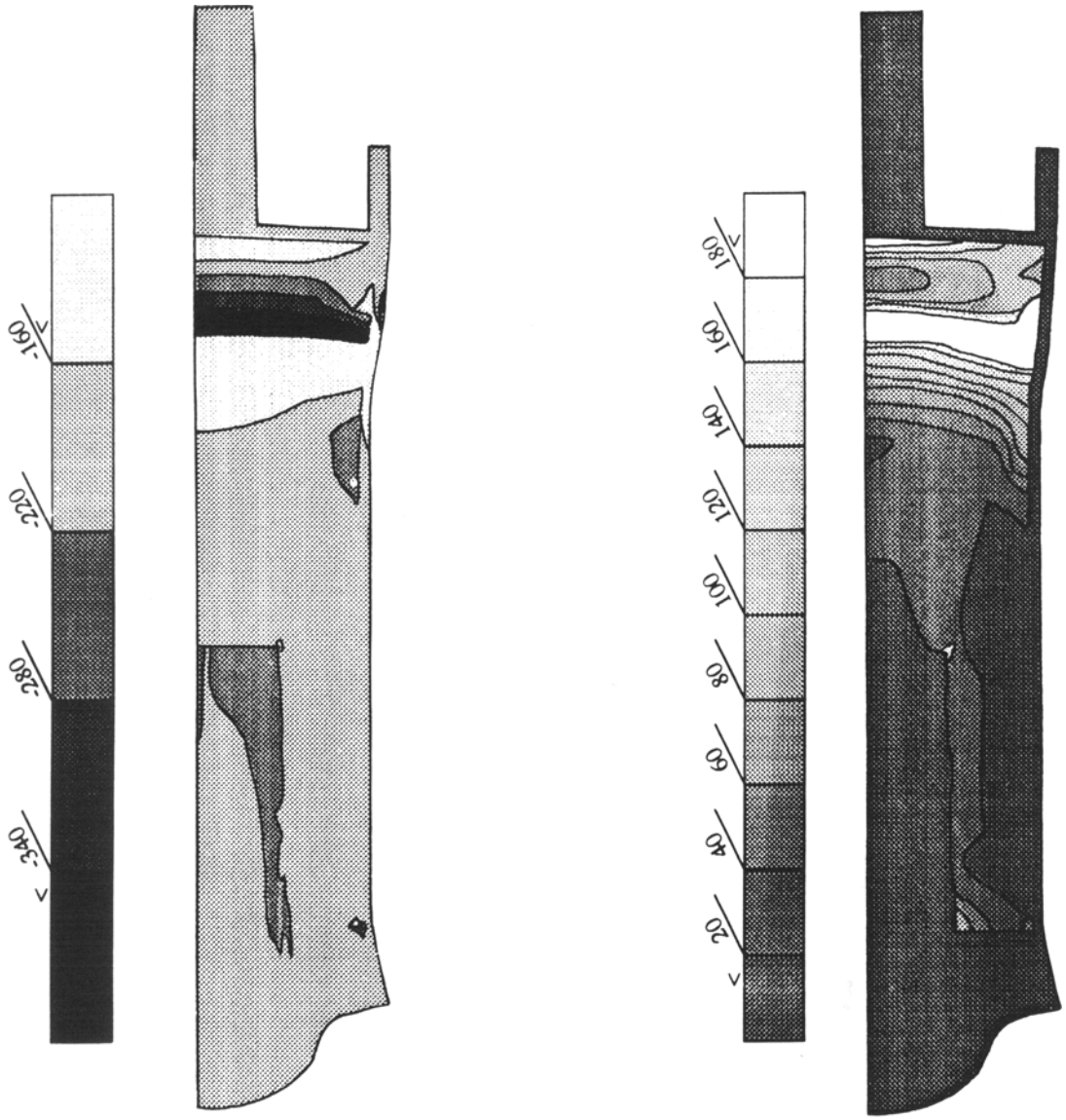

(a) (b)

Fig. 15 Stress maps (MPa) at the beginning of the HIP dwell (titanium core). **(a)** Pressure ($I_1/3$). **(b)** Shear ($\sqrt{3J_2}$).

Table 4 Comparison of Computed and Observed Final Dimensions (mm)

	Initial	Observed	Computed
Graphite core			
External diameter	39.8	33.8	33.1
Height	54.4	46.0	45.9
Minimum axial thickness	17.4	12.7	12.9
Titanium core			
Smaller diameter (hole)	20.0	17.8	16.6
Larger diameter (hole)	22.0	19.6	19.2
Height (hole)	35.0	29.0	29.4
External smaller diameter (crucible)	40.0	32.6	32.5
External larger diameter (crucible)	40.0	37.0	36.9
Height (crucible)	74.0	60.0	60.5

residual stresses were calculated. Experimental final shapes were compared with predicted ones, showing good agreement (see Table 4). It was shown that the titanium insert has a very limited effect on the densification of the TiB_2 powder. On the other hand, nondeformable inserts such as graphite play an important role.

References

1. R. Raj, *J. Am. Ceram. Soc.*, Vol 65 (No. 3), 1982, p C46.
2. K.R. Venkatachari and R. Raj, *J. Am. Ceram. Soc.*, Vol 69 (No. 6), 1986, p 499-506.
3. P.C. Panda, J. Lagraff, and R. Raj, *Acta Metall.*, Vol 36 (No. 8), 1988, p 1929-1939.

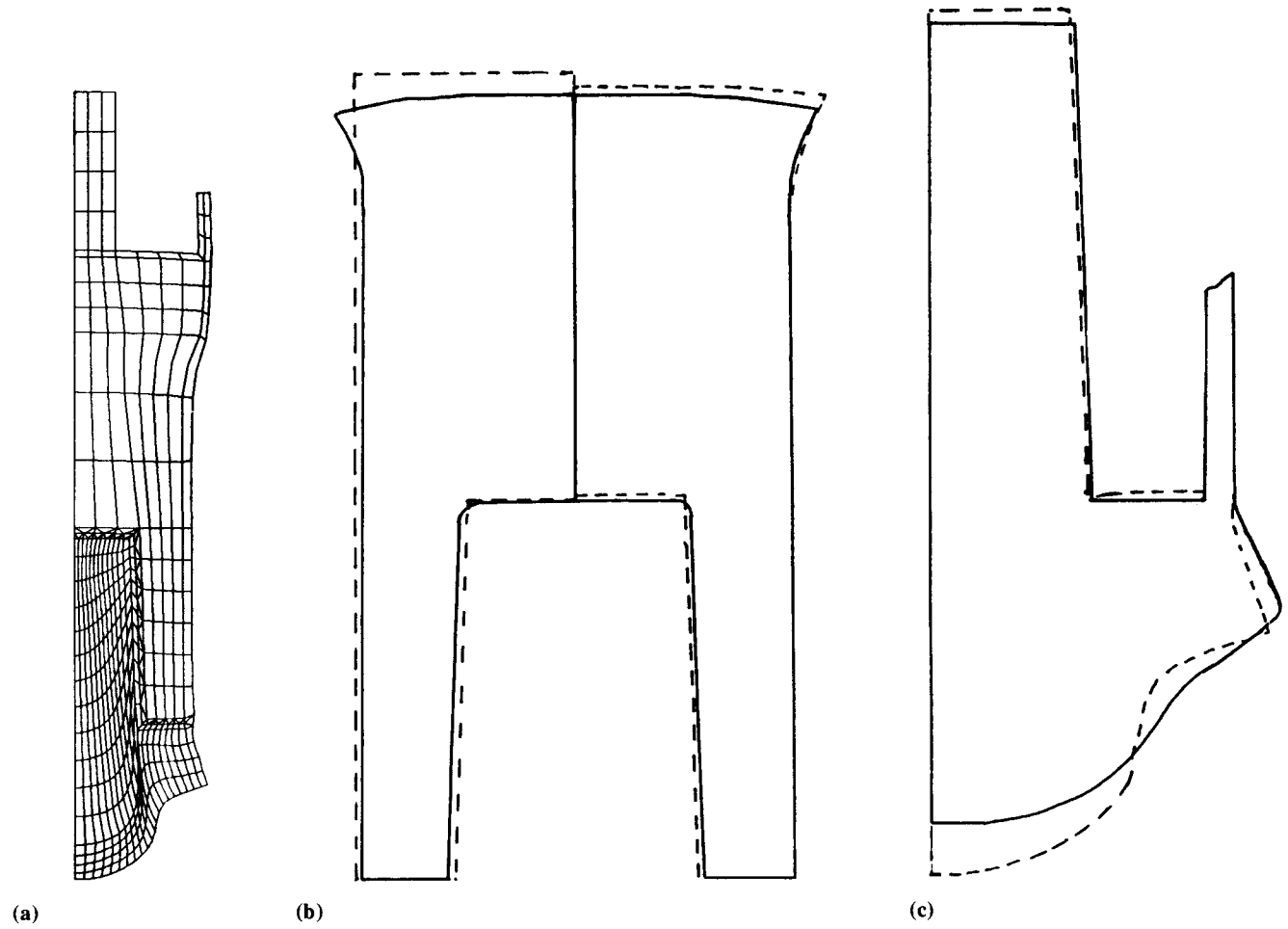

Fig. 16 (a) Final calculated part. (b) Comparison of the calculated (dashed line) and the experimental (solid lines) final shape of the crucible using FEM analysis (right) and isotropic shrinkage hypothesis (left). (c) Comparison of the calculated (dashed line) and the experimental (solid lines) final shape of the bulging part of the container (FEM calculation).

4. R.K. Bordia and G.W. Scherer, *Acta Metall.*, Vol 36 (No. 9), 1988, p 2393-2397.
5. R.K. Bordia and G.W. Scherer, *Acta Metall.*, Vol 36 (No. 9), 1988, p 2399-2409.
6. G.W. Scherer, *J. Am. Ceram. Soc.*, Vol 60 (No. 5-6), 1977, p 236-239.
7. R.M. McMeeking and L.T. Kuhn, *Acta Metall. Mater.*, Vol 40 (No. 5), 1992, p 961-969.
8. J.M. Duva and P.D. Crow, *Acta Metall. Mater.*, Vol 40 (No. 1), 1992, p 31-35.
9. A.L. Gurson, *J. Eng. Mater. Technol., Trans. ASME*, Vol 99, 1977, p 2-15.
10. H.A. Kuhn and C.L. Downey, *Int. J. Powder Metall.*, Vol 7 (No. 1), 1971, p 15-25.
11. M. Abouaf, J.L. Chenot, G. Raisson, and P. Bauduin, *Int. J. Num. Meth. Eng.*, Vol 25 (No. 1), 1988, p 191-212.
12. A. Nohara, T. Soh, and T. Nakagawa, *Int. J. Num. Meth. Eng.*, Vol 25 (No. 1), 1988, p 213-225.
13. S. Shima and M. Oyane, *Int. J. Mechan. Sci.*, Vol 18, 1976, p 285-291.
14. D. Bouvard and M. Lafer, in *Advances in Powder Metallurgy*, Vol 1, Metal Powder Industries Federation, 1989, p 491-503.
15. J. Duszczyk, *J. Mater. Shaping Technol.*, Vol 9, 1991, p 103-115.
16. J. Duszczyk and L. Kowalski, *J. Mater. Shaping Technol.*, Vol 8, 1990, p 225-237.
17. J. Besson, M. Abouaf, F. Mazerolle, and P. Suquet, in *Creep in Structures*, M. Życzkowski, Ed., 4th IUTAM Symp., Cracow, Poland, 10-14 Sept 1990, p 45-53.
18. J. Besson and M. Abouaf, *J. Am. Ceram. Soc., 75*(8), 1992, p 2165-2172.
19. S. Shima and K. Mimura, *Int. J. Mech. Sci.*, Vol 28 (No. 1), 1986, p 53-59.
20. D.S. Wilkinson and M.F. Ashby, *Acta Metall.*, Vol 23, 1975, p 1277-1285.
21. A.S. Helle, K.E. Easterling, and M.F. Ashby, *Acta Metall.*, Vol 33 (No. 12), 1985, p 2163-2174.
22. W.G. Moffatt, *The Handbook of Binary Phase Diagrams*, General Electric Company, 1978.
23. H.R. Baumgartner and R.A. Steiger, *J. Am. Ceram. Soc.*, Vol 67 (No. 3), 1984, p 207-212.
24. P.F. Becher, C.F. Finch, and M.K. Ferber, *J. Mater. Sci. Lett.*, Vol 5, 1986, p 195-197.
25. C.B. Finch, P.F. Becher, P. Angelini, S. Baik, C.E. Bamberger, and J. Brynestad, *Advanced Ceramic Mater.*, Vol 1, 1986, p 50-54.
26. R.C. Dorward, *J. Mater. Sci. Lett.*, Vol 4, 1985, p 694-696.

27. M.K. Ferber, P.F. Becher, and C.B. Finch, *J. Am. Ceram. Soc.*, Vol 66, 1983, p C2-C3.
28. H. Riedel, Fracture at High Temperature, in *Materials Research and Engineering*, B. Ilschner and N.J. Grant, Ed., Springer-Verlag, 1986.
29. P. Chantikul, G.R. Anstis, B.R. Lawn, and D.B. Marshall, *J. Am. Ceram. Soc.*, Vol 64 (No. 9), 1981, p 539-543.
30. A.G. Evans and C.H. Hsueh, *J. Am. Ceram. Soc.*, Vol 69 (No. 6), 1986, p 444-448.
31. J. Besson and M. Abouaf, *Acta Metall. Mater.*, Vol 39 (No. 10), 1991, p 2225-2234.
32. L.T. Kuhn, R.M. McMeeking, and F.F. Lange, *J. Am. Ceram. Soc.*, Vol 73 (No. 3), 1991, p 682-685.
33. M.S. Koval'chenko and M.M. Mai, *Sov. Powder Metall. Met. Ceramic*, 1973, p 622-625.
34. M.S. Koval'chenko, L.F. Ochkas, and V.B. Vinokurov, *J. Less-Common Met.*, Vol 67, 1979, p 297-301.
35. E.V. Clougherty, R.L. Pober, and L. Kaufman, in *Modern Developments in Powder Metallurgy*, Vol 2, H.H. Hausner, Ed., Plenum Press, 1965, p 321-329.
36. H.J. Frost and M.F. Ashby, *Deformation Mechanisms Maps*, Pergamon Press, Oxford.
37. M. Boncoeur and F. Valin, *Brevet Français*, Vol 89, 1989, p 15479.
38. J. Besson and M. Abouaf, *Int. J. Solids Structures*, Vol 28 (No. 6), 1991, p 691-702.
39. R.M. McMeeking, *Int. J. Mech. Sci.*, Vol 34 (No. 1), 1992, p 53-62.
40. J. Xu and R.M. McMeeking, *Int. J. Mech. Sci.*, Vol 34 (No. 2), 1992, p 167-174.
41. S. Langman, Wrought Titanium and Titanium Alloys, *Metals Handbook*, ASM International, Vol 2, 10th ed., 1990, p 592-633.
42. R. Hill, *Mathematical Theory of Plasticity*, Oxford University Press, 1950, p 106-114.